JOURNAL OF
APPLIED
CRYSTALLOGRAPHY

Volume 57 (2024)

Supporting information for article:

A TEM study of the crystallographic characteristics of magnetite needles in plagioclase: role of the quasi-close-packed oxygen sublattice in plagioclase structure

Shyh-Lung Hwang, Pouyan Shen, Tzen-Fu Yui, Hao-Tsu Chu and Yoichi Usui

The proper indexing for the ODF plots of Ageeva et al. (2020)

It is in fact difficult to read crystallographic information from the ODF plots in Figs. 2(*d*) and 2(*e*) of Ageeva *et al*. (2020), as the poles from various magnetite groups are severely overlapped, especially in $<111>_m$ projections. However, by abiding to some “distinct” crystallographic descriptions for the specific needle groups in Table 1 of Ageeva *et al.* (2020) and starting with the indexing of $\{011\}_m$ poles solely from the single magnetite groups, the ODF plots in Ageeva *et al*. (2020) were properly indexed. For example, starting with $\{110\}_m$ // $(1\bar{5}0)_p$ as described in Ageeva *et al.* (2020) for the “main orientation” of pl(112)n-mt group, a self-consistent set of $\{110\}_m + \{111\}_m$ poles are obtained [red circles in Figs. S1(*a*) and S1(*b*)]. Such indexing contains two independent $\{110\}_m$ poles and two independent $\{111\}_m$ poles not overlapped with the poles from other needle groups, and therefore most likely is correct. By the similar approach, the sets of $\{110\}_m + \{111\}_m$ poles for all 6 main needle groups [each with >5 analyses; see red, yellow, green, indigo, blue or black circles in Figs. S1(*a*) and S1(*b*)], as well as 15 trivial groups, were properly indexed as described below as item 1-8. [Note that the labeling of (150) and $(\bar{5}1\bar{8})$ in Fig. 2 of Ageeva *et al.* (2020) should be corrected as $(\overline{15}0)$ and $(5\bar{1}8)$, in order to be consistent with the other labelings for the plagioclase host.]

1. The set of yellow poles with the COR: $<011>_m$ // $[001]_p$ & $\{1\bar{1}1\}_m$ // $(1\bar{5}0)_p$ are in accordance with the crystallographic descriptions on the “main orientation” of pl[001]-mt group in Ageeva *et al.* (2020) and the same as that of [001]-needle in this work (Figs. S1*a* and S1*b*; see also stereogram in Fig. 6*a* and Table 1).

2. The set of minor black poles with the COR: $\{111\}_m$ // $(100)_p$ & $\{111\}_m$ // $(\bar{1}50)_p$ in are in accordance with the crystallographic descriptions on the "main orientation" of the pl(100)n-mt group in Ageeva *et al.* (2020). However, such a COR is in fact quite similar to that of $\mathbf{\bar{1}50^*}$a-needle in this work (Figs. S1*a* and S1*b*; see also stereogram in Fig. 6*g* and Table 1), thereby render the crystallographic descriptions on the pl(100)n-mt group in Ageeva *et al*. (2020) a pending issue for future analyses.

3. In Table 1 of Ageeva *et al*. (2020), only pl[001]-mt, pl(100)n-mt, and pl($1\bar{5}0$)n-mt have a $\{111\}_m$ plane in "alignment" to $(1\bar{5}0)_p$. So, the set of green poles with the COR: $<111>_m \wedge \mathbf{1\bar{5}0^*}_p = \sim 7°$ & $\{0\bar{1}1\}_m \wedge (112)_p = \sim 27°$ would correspond to the pl($1\bar{5}0$)n-mt group (Figs. S1*a* and S1*b*). [The small but definite ~7° systematic (not random) mis-alignment between NA and $\mathbf{1\bar{5}0^*}_p$ could be vividly seen in $<011>_m$ projections by the apparent offset between the trace of $(1\bar{5}0)_p$ plane (dotted big-circle $1\bar{5}0$t in Fig. S1*b*) and the trace of $\{111\}_m$ plane (green big-circle in Fig. S1*b*)]. Such crystallographic characteristics after the properly indexed ODF plots, especially along the lateral direction, are in contradiction with the COR: NA // $<111>_m$ // $\mathbf{1\bar{5}0^*}_p$ & $\{0\bar{1}1\}_m$ // $(112)_p$ as described for the "main orientation" of the pl($1\bar{5}0$)n-mt group in Ageeva *et al.* (2020). In other words, except for a minor #5 group with $<111>_m$ // $\mathbf{1\bar{5}0^*}_p$ (Fig. S1*a*), the majorities of pl($1\bar{5}0$)n-mt needles in the properly indexed ODF plots are not elongated exactly along the normal of $(1\bar{5}0)_p$ plane, and are not bounded by the $\{0\bar{1}1\}_m$ // $(112)_p$ lateral facets, *i.e.* not as described in Ageeva *et al*. (2020). This pl($1\bar{5}0$)n-mt group apparently corresponds to the $\mathbf{1\bar{5}0^*}$b-needle in this work (see stereogram in Fig. 6*h* and Table 1).

4. The set of red poles with the COR: $<111>_m \wedge \mathbf{112^*}_p = \sim 10°$ & $\{011\}_m$ // $(\bar{1}50)_p$ does not meet the description $<111>_m$ // $\mathbf{112^*}_p$ for "general orientation" or "main orientation" of the pl(112)n-mt group in Ageeva *et al*. (2020). [The ~10° systematic (not random) mis-alignment

between $\langle 111\rangle_m$ and $\mathbf{112^*}_p$ could be clearly seen in $\{011\}_m$ projections by the apparent offset between the trace of 112_p plane (dotted big-circle 112t in Fig. S1*b*) and the trace of $\{111\}_m$ plane (red big-circle in Fig. S1*b*)]. However, except for a larger axial mis-alignment along NA, *i.e.* ~10°, this group of magnetites in the ODF plots apparently corresponds to the **112***a-needle in this work (see stereogram in Fig. 6*b* and Table 1).

Whereas the above pl(112)n-mt needles (red poles) are characterized by $\{110\}_m$ // $(\bar{1}50)_p$ but without $\langle 111\rangle_m$ // $\mathbf{112^*}_p$, the other pl(112)n-mt needles are characterized by $\langle 111\rangle_m$ // $\mathbf{112^*}_p$ but without $\{110\}_m$ // $(\bar{1}50)_p$. Such needles show the axial alignment along lateral directions, *e.g.* $\langle 011\rangle_m$ // $[4\bar{2}\bar{1}]_p$ (#3 small pink poles), $\langle 011\rangle_m$ ~//~ $[0\bar{2}1]_p$ (#4 small pink poles), or $\langle 011\rangle_m$ ~// $[\bar{1}10]_p$ (indigo poles) (Figs. S1*a* and S1*b*), with the last two indicated in footnotes of Table 1 in Ageeva *et al*. (2020). The $\{011\}_m$ poles of such needle groups are lying on the big-circle centered at 112_p pole (Fig. S1*b*), indicating that their NAs are indeed in alignment to $\mathbf{112^*}_p$ (Fig. S1*a*), *i.e.* following the “general orientation” of pl(112)n-mt group, as described in Ageeva *et al*. (2020). These needles with ~16-40° mis-alignment between $\{110\}_m$ and $(\bar{1}50)_p$ apparently correspond to the **112***c-needle in this work (see stereogram in Fig. 6*d* and Table 1). [Note that such set of data with $\langle 111\rangle_m$ // $\mathbf{112^*}_p$ but without $\{011\}_m$ // $\bar{1}50_p$ from the “equal-area” stereogram in Figs. 2*d* and 2*e* of Ageeva *et al.* (2020) are quite similar to the data in the “equal-angle” stereogram of Ageeva *et al.* (2022) (Fig. S1*c* modified from Fig. 2*b* in Ageeva *et al*., 2022)]. In summary, except probably for the few needles indicated by red arrow in Fig. S1*c*, the majorities of pl(112)n-mt needles in the EBSD analyses of Ageeva *et al*. (2020, 2022) do not follow the “main orientation” with $\langle 111\rangle_m$ // $\mathbf{112^*}_p$ & $\{011\}_m$ // $\bar{1}50_p$.

5. The set of blue poles with the COR: $\langle 111\rangle_m \wedge \mathbf{\bar{3}12^*}_p$ = ~5° & $\{0\bar{1}1\}_m \wedge (150)_p$ = ~16° is the only possible candidate in the ODF plots to be assigned as the pl($\bar{3}$12)n-mt group in Ageeva *et al*. (2020). [The small but definite ~5° mis-alignment along NA could be better

seen in $\{011\}_m$ projections by the apparent offset between the trace of $\bar{3}12_p$ plane (dotted big-circle $\bar{3}12$t in Fig S1*b*) and the trace of $\{111\}_m$ plane (blue big-circle in Fig. S1*b*)]. Except for a single #6 needle to be addressed in item 7, the ODF plots of Ageeva *et al*. (2020) probably contain no magnetite crystals that fully meet the crystallographic descriptions for the pl($\bar{3}$12)n-mt group.

6. The remaining four minor groups, *i.e.* #1, #2, #2b & #7 with $<111>_m \wedge$ $\mathbf{150^*}_p$ = ~0-7° & $\{011\}_m \wedge (\bar{3}12)_p$ = ~14-25° (Figs. S1*a* and S1*b*) likely correspond to the pl(150)n-mt group in Ageeva *et al.* (2020). Apparently there are probably no pl(150)n-mt needles in the properly indexed ODF plots that follow the "main orientation" with $<111>_m$// $\mathbf{150^*}_p$ & $\{011\}_m$ // $(\bar{3}12)_p$ as described in Ageeva *et al.* (2020).

7. Ageeva *et al*. (2020) reported magnetites with the "nucleation orientation", *i.e*. with one $<111>_m$ being parallel to the needle growth direction and one $<001>_m$ parallel to $[\overline{14}\ \overline{10}\ \bar{7}]_p$ or $[14\ \overline{10}\ 7]_p$ for all 6 main magnetite needles in EBSD analyses (see Table 1 of Ageeva *et al*., 2020). Since the intra-angle between $<001>_m$ and $<111>_m$ is 54.5°, any magnetite inclusion(s) following the "nucleation orientation" would have all four $\{111\}_m$ poles simultaneously disposed along the small circles with 54.5° semi-angle centered at $[\overline{14}\ \overline{10}\ \bar{7}]_p$ or $[14\ \overline{10}\ 7]_p$ pole. As can be clearly seen in Fig. S1*a*, among all 92 magnetite inclusions analyzed in Ageeva *et al*. (2020), only a trivial #6 group (blue small circles) and the pl(100)n-mt group have all four $\{111\}_m$ poles tightly and loosely, respectively, confined by the 54.5° small circle centered at $[14\ \overline{10}\ 7]_p$ pole. In other words, among the 92 analyses in Ageeva *et al.* (2020), there are probably no pl(112)n-mt, pl(1$\bar{5}$0)n-mt, pl(150)n-mt, or pl[001]-mt needles at the "nucleation orientation".

8. The <111>$_m$ directions of the #8 ~ #14 trivial groups seem to be randomly oriented in the plagioclase host (Fig. S1*a*). This suggests that among the 92 magnetites in the ODF plots of Ageeva *et al*. (2020), some of them might be the "equaxed magnetites" or "mist crystals" in random orientations to the plagioclase host (see Fig. 2*d*−2*f* of Ageeva *et al*., 2022).

Figure S1 The properly indexed ODF plots of Ageeva *et al.* (2020)

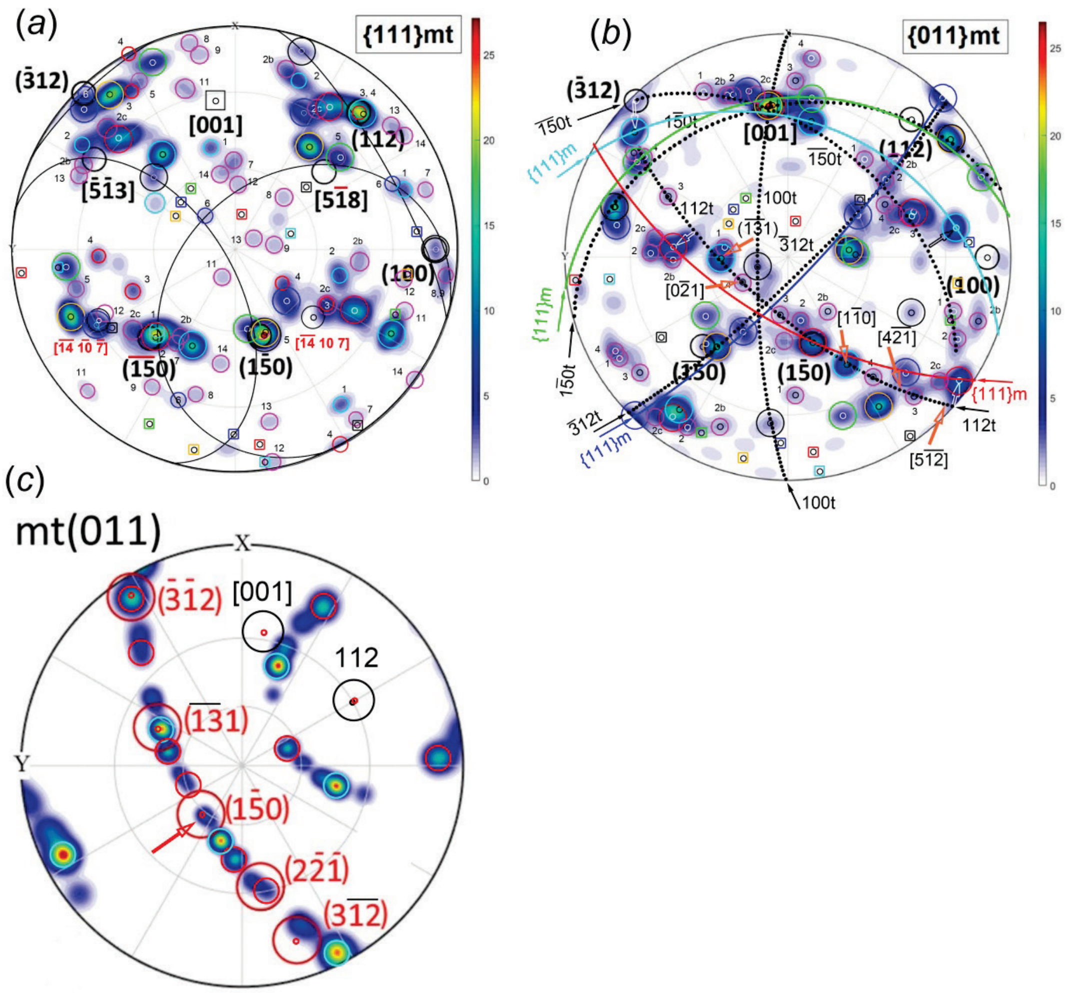

Figure S1. (a,b) The properly indexed equal-area ODF plots modified/reproduced with permission from Figs. 2(*d*) and 2(*e*) of Ageeva *et al*. (2020), (c) the equal-angle ODF plot modified/reproduced from Fig 2(*b*) of Ageeva *et al.* (2022), and (d) the stereograms retrieved from (a) showing the $\{001\}_m \pm \{111\}_m$ poles of all needle-groups in colors. The 6 set of magnetite poles as concerned in this study are respectively marked by red, indigo, green, blue, yellow and black circles. Note that the inconsistent labeling of (150) and $(\bar{5}1\bar{8})$ Figs. 2(*d*) and 2(*e*) of Ageeva *et al.* (2020) is corrected as $(\bar{1}50)$ and $(5\bar{1}8)$ in (a,b), and the inconsistent labeling of $(13\bar{1})$ and $(\bar{3}12)$ in Fig 2(*b*) of Ageeva et al. (2022) is corrected as $(\bar{1}\bar{3}1)$ and $(3\bar{1}\bar{2})$ in (c). (Notation t: trace).

Figure S2 112*-needles

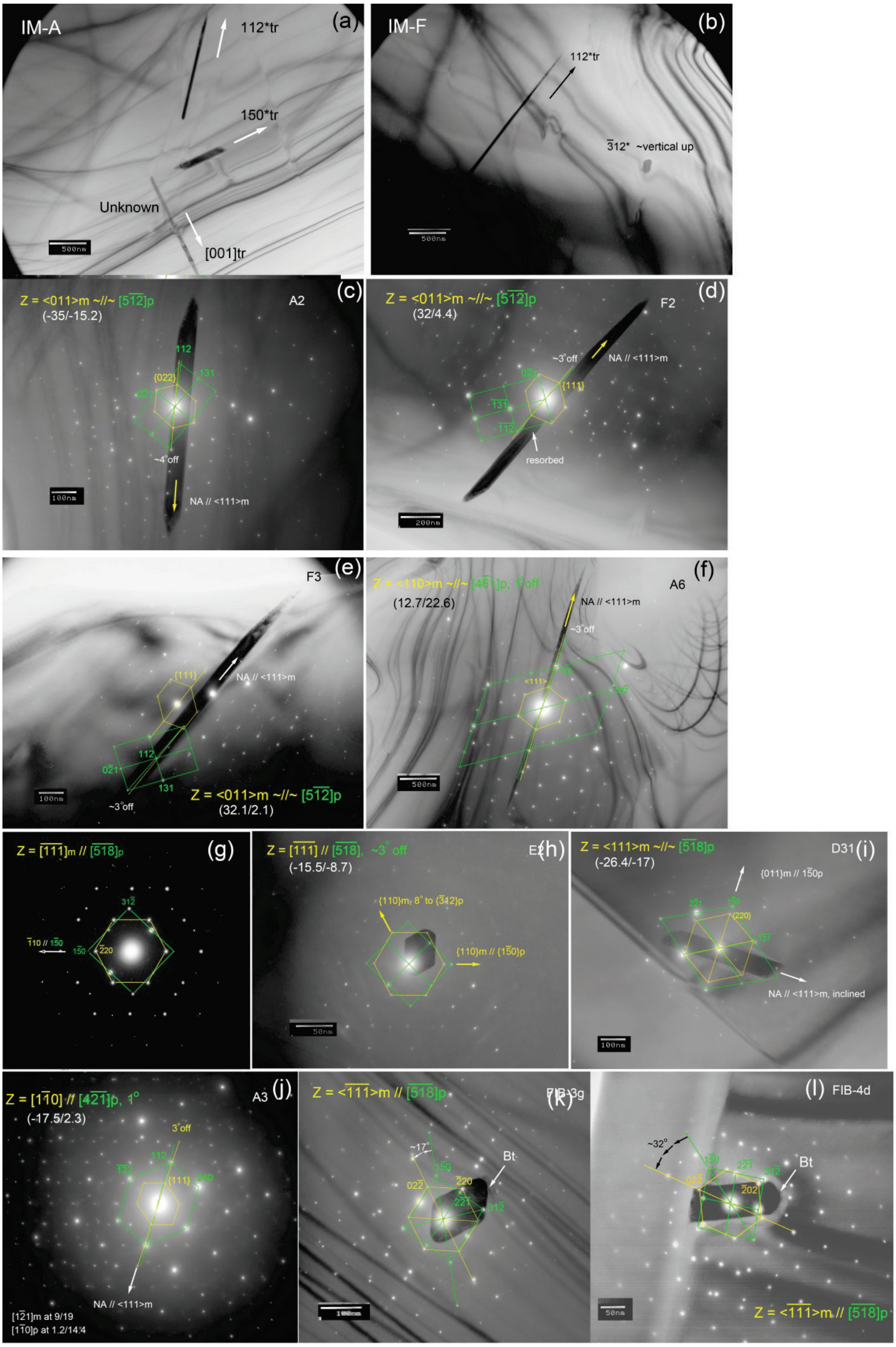

Fugure S2. (a,b) TEM BFI showing the characteristic size differences between **112***-needle and other needle variants, (c-i) TEM BFIs with superimposed SAED patterns or SAED pattern of **112***a-needles with NA (c-f) parallel, (g,h) normal, (i) at ~71° inclination to image plane showing (c-f) NA // $<111>_m$ & NA ∧ **112***$_p$ = ~3-4°, (g,h) the COR: $[111]_m$ // $[518]_p$ & $(\bar{1}10)_m$ // $(1\bar{5}0)_p$ and the cross-section bounded by $(\bar{1}10)_m$ // $(1\bar{5}0)_p$ + other $\{110\}_m$ facets, (i) the characteristic $<111>_m$ ~//~$[\bar{5}\bar{1}8]_p$ sub-alignment and the exact $\{110\}_m$// $(1\bar{5}0)_p$ alignment. (j-l) TEM BFIs with superimposed SAED patterns or SAED pattern of **112***c-needles with NA (j) parallel, (k,l) normal to image plane showing (j) NA // $<111>_m$ and the axial sub-alignment $<011>_m$ ~//~ $[\bar{4}21]_p$, (k,l) the $\{110\}_m$ facets with mis-alignment in terms of $\{011\}_m$ ∧ $1\bar{5}0_p$ = ~17° or ~32°. (The X and Y tilt angles of the TEM specimen holder are noted in parentheses.)

Figure S3 $\bar{3}$12*-needles

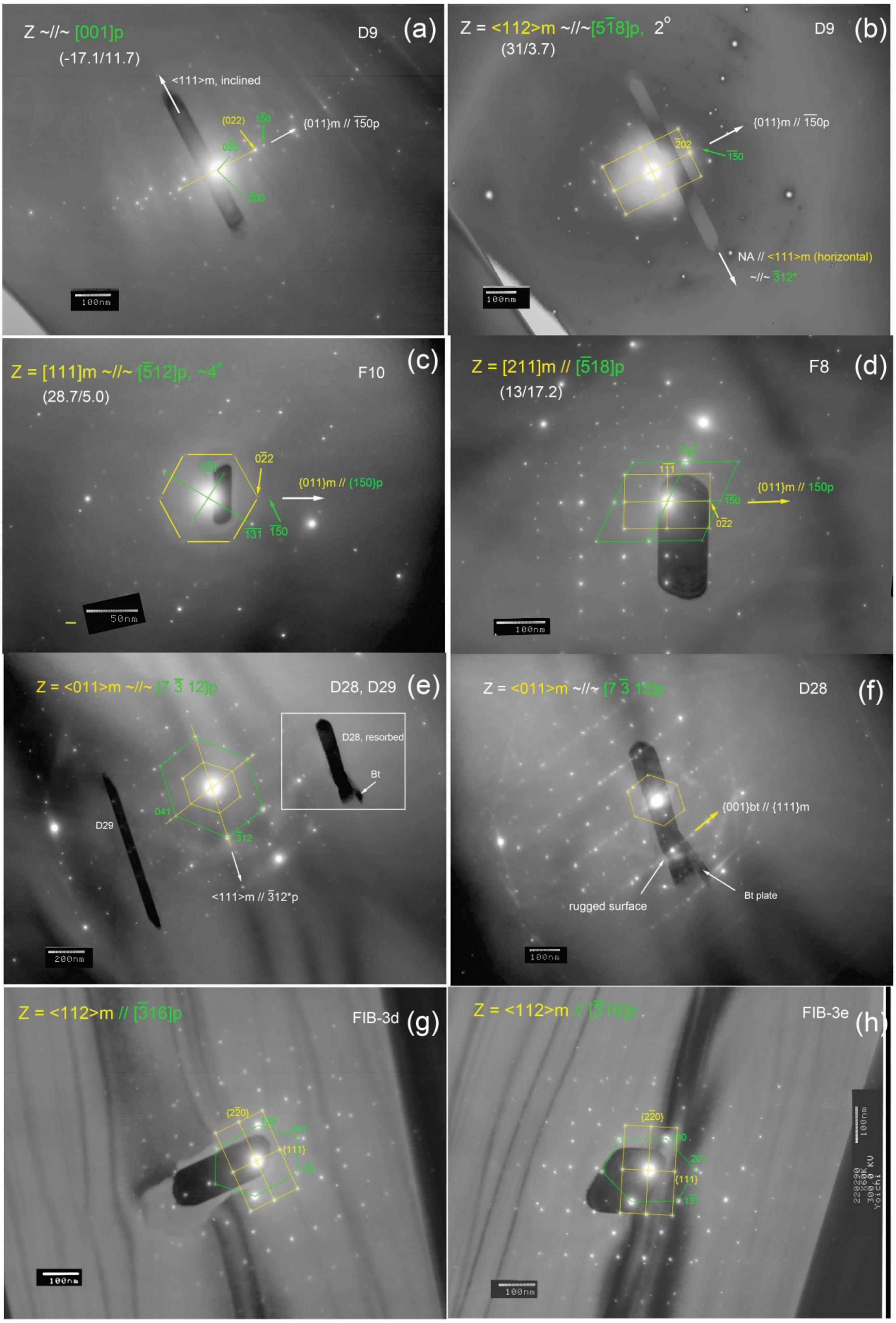

Figure S3. (a-d) TEM BFIs with superimposed SAED patterns of $\mathbf{\bar{3}12^*}$a-needles with NA (a,b) parallel, (c) normal, (d) inclined to image plane showing (a,b) NA // <111>$_m$, (c) the facetted cross-sections bounded by the large, well-developed $\{011\}_m$ // $\{150\}_p$ facets in <111>$_m$ ~//~ $[\bar{5}12]_p$ zone-axis, (d) the well-developed $\{011\}_m$ // $\{150\}_p$ facets in <211>$_m$ ~//~ $[\bar{5}18]_p$ zone axes. (e-h) TEM BFIs with superimposed SAED patterns of $\mathbf{\bar{3}12^*}$c-needles with NA (e,f) parallel, (g,h) at 60° inclination to the image plane showing (e,f) NA // <111>$_m$ // $\mathbf{\bar{3}12^*}_p$ and the characteristic resorbed outlines with mica overgrowths, (g,h) the COR: <112>$_m$ // $[\bar{3}16]_p$ & $(111)_m$ // $(201)_p$ (5° off) and the characteristic cross-sections bounded by $\{110\}_m$ facets.

Figure S4 $\bar{1}$50* and 150*-needles

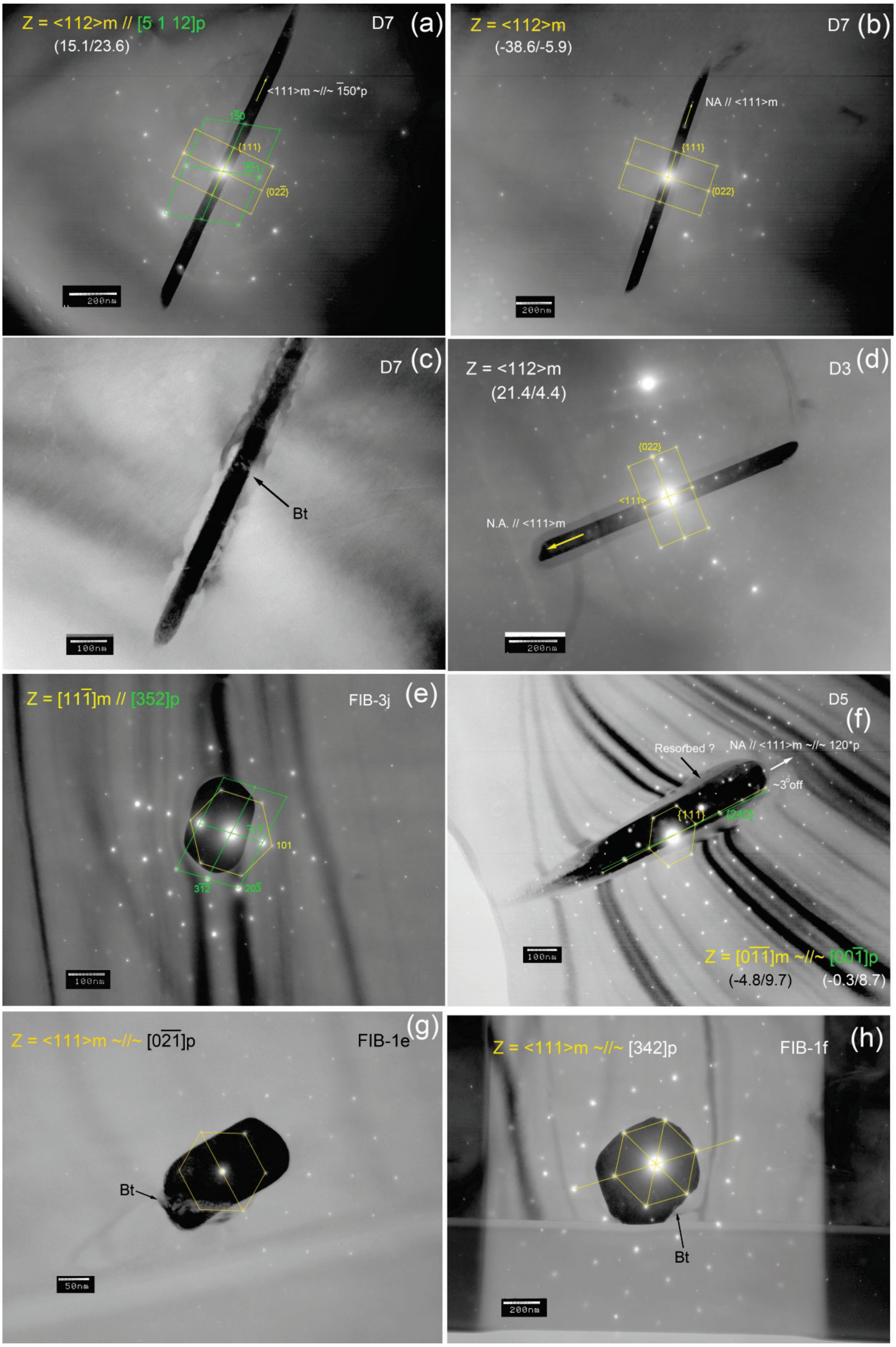

Figure S4. (a-c) TEM BFIs with superimposed SAED patterns of $\bar{\mathbf{1}}$**50***a-needles with NA parallel to image plane showing (a,b) the exact alignment between NA and <111>$_m$ lattice direction, (c) the constant presence of mica overgrowths on needle surface. TEM BFIs with superimposed SAED patterns of (d) **150***a-needle with NA parallel to image plane showing NA // <111>$_m$, and (e) **150***b-needle at end-on orientation showing the {110}$_m$ facetted cross-section and the COR: $[11\bar{1}]_m$ // $[352]_p$, $(101)_m$ // $(\bar{1}1\bar{1})_p$. (f-h) TEM BFIs with superimposed SAED patterns of **150***r-needles with NA (f) parallel to image plane, (g.h) end-on showing the the resorbed outlines and mica associations.

Figure S5 mica plates in plagioclase

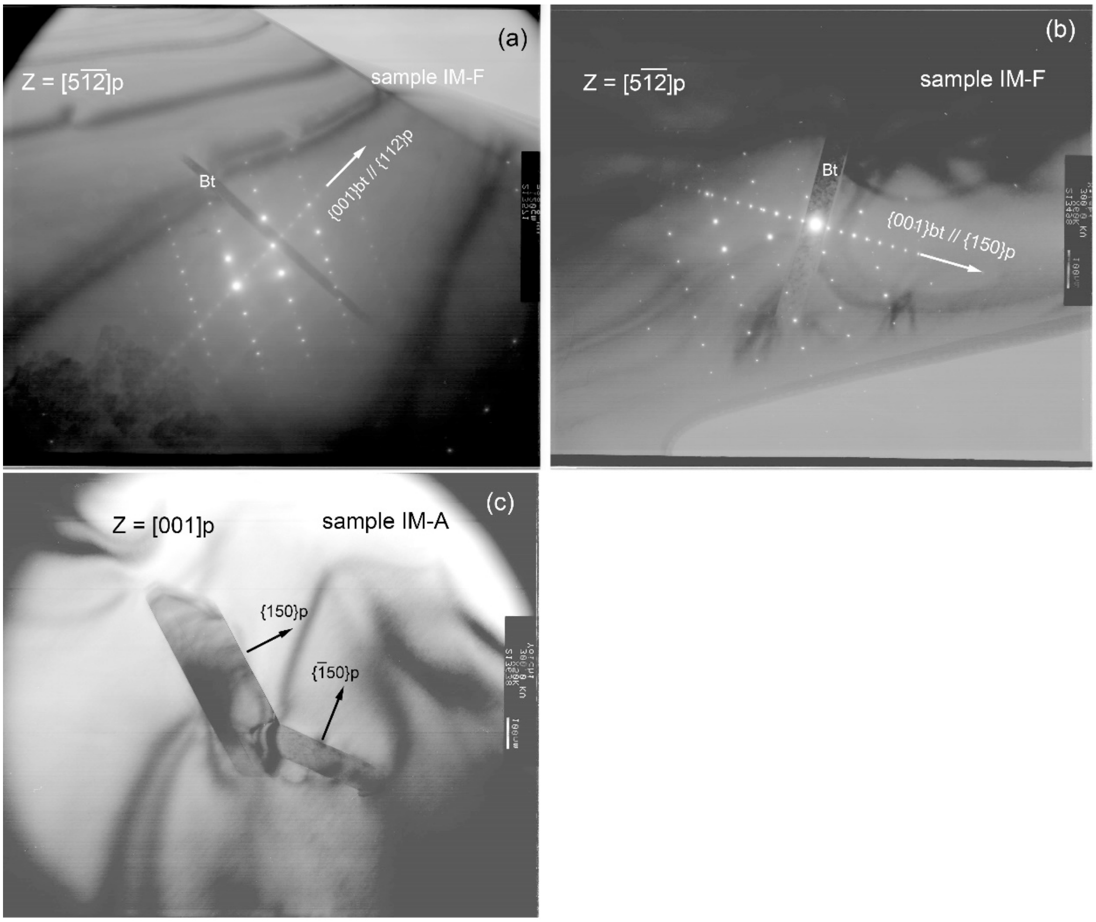

Figure S5. TEM BFI and SAED pattern showing 001 mica plates lying parallel to (a) 112_p, (b) 150p, and (c) 150_p and $\bar{1}50_p$.

Figure S6 rutile and ilmenite in labradorite stones

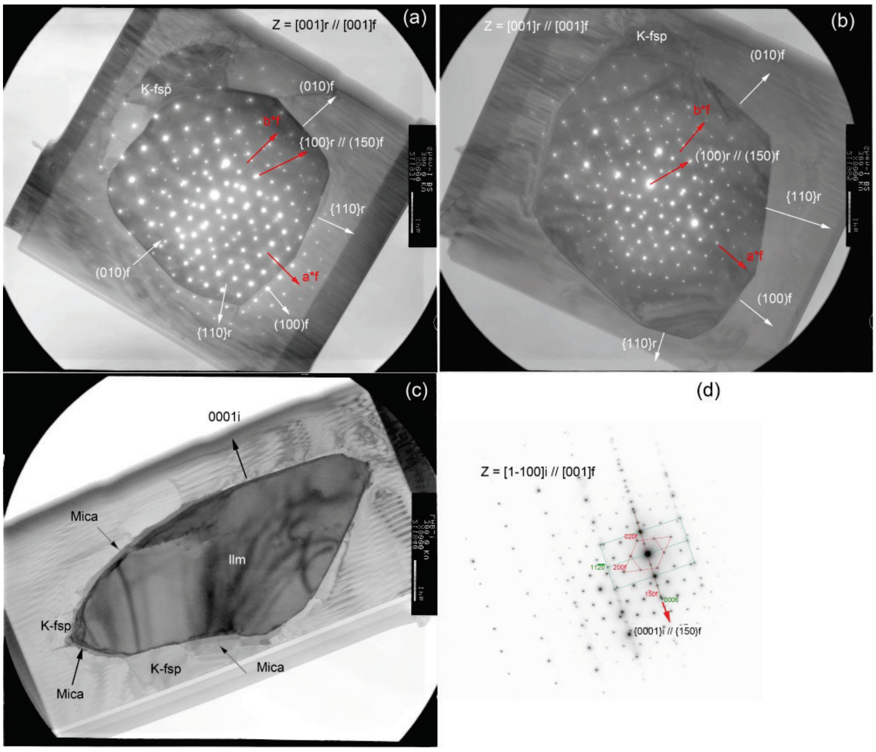

Figure 6. TEM BFIs and corresponding SAED patterns showing quasi-cp $\{150\}_p$ or $\{\bar{1}50\}_p$ oxygen plane of feldspar (f) is aligned with (a,b) quasi-cp $\{100\}_r$ oxygen plane of the $[001]_r$ // $[001]_f$-oriented rod-like rutile (r) inclusion, and (c,d) cp $\{0001\}_i$ oxygen planes of the $[1\bar{1}00]_r$ // $[001]_f$-oriented blade-like ilmenite (i) inclusion in commercial labradorite stones.

Figure S7 TO_4 polyhedral projections of feldspar

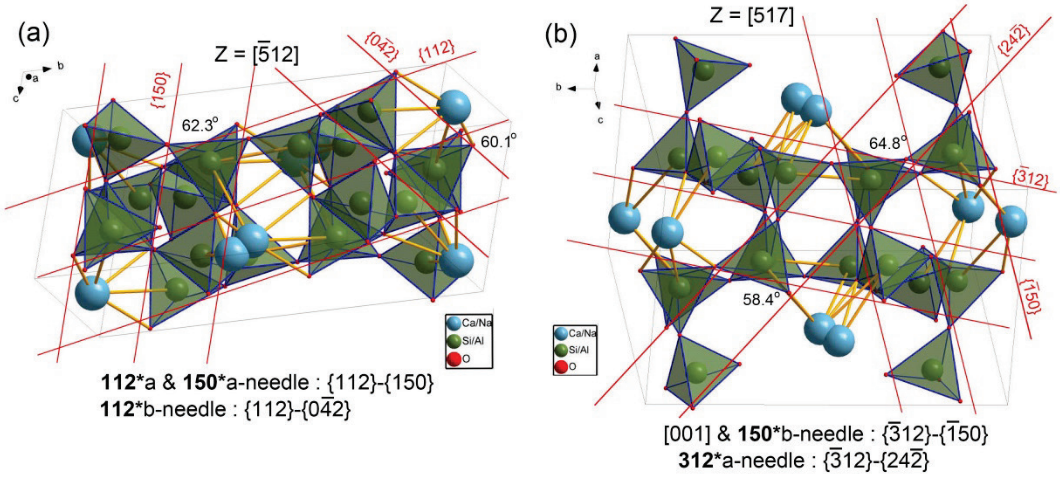

Figure 1. Plagioclase structure projections along (a) $[\bar{5}12]_p$ and (b) $[517]_p$ directions showing TO4 polyhedra bounded by (a) 112_p, 150_p, and $0\bar{4}2_p$ planes, and (b) $\bar{3}12_p$, $\bar{1}50_p$, and $24\bar{2}_p$ plane.

Figure S8 JEM-3010 calibration

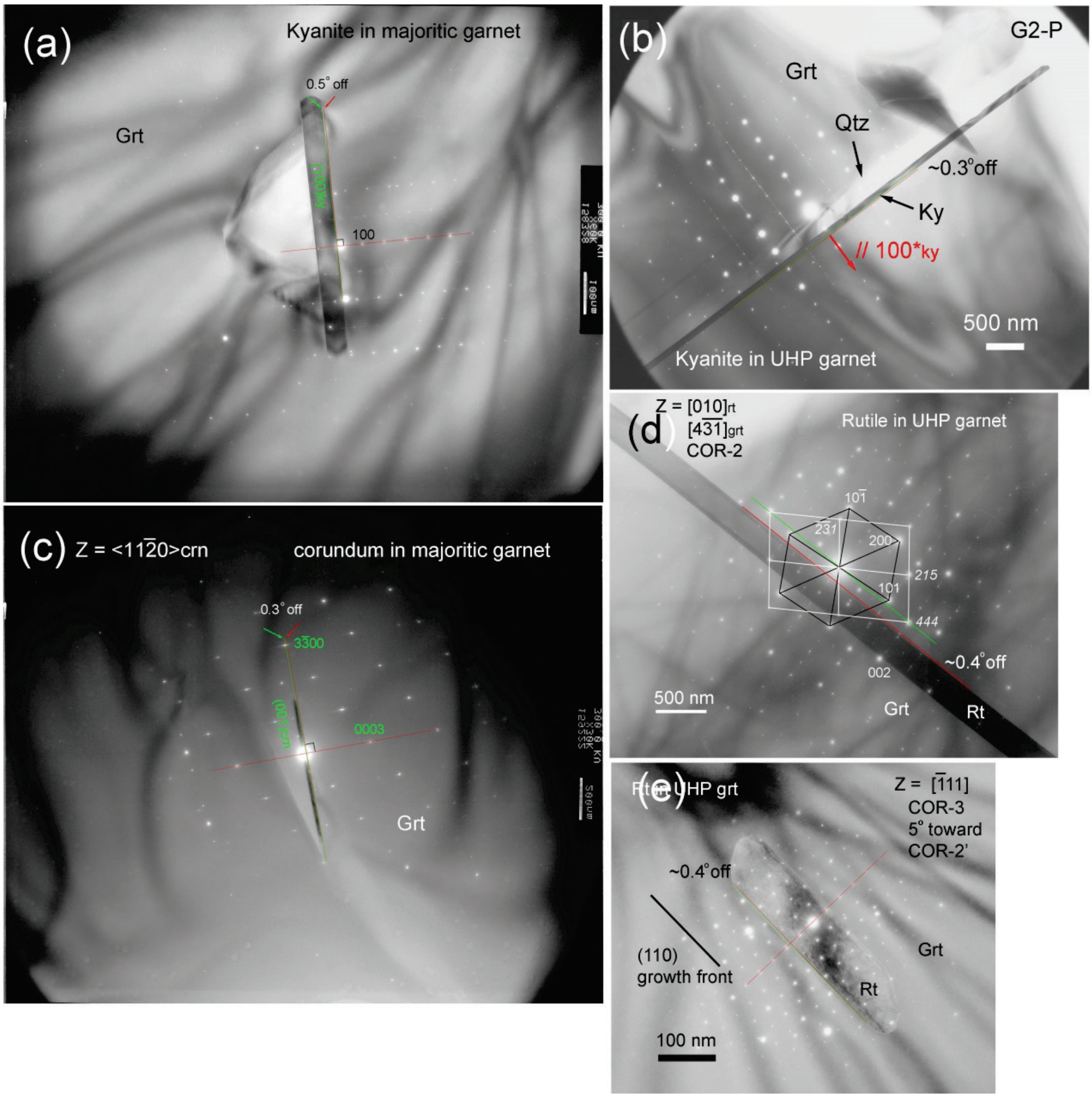

Figure 8. (a-e) TEM images and the associated SAED patterns of (a,b) 100 kyanite plates in majoritic or UHP garnets, (c) 0001 corundum plate, and (d, e) $\langle 111 \rangle_{grt}$-oriented rutile needles with the characteristic $\{011\}_{grt}$ facets, nicely demonstrating that the possible systematic misalignments between images at ≤150K magnifications and the corresponding diffraction patterns at 120 or 150 cm cameral lengths are ≤ 0.5° by the JEOL-3010 instrument operated at 300 KeV.

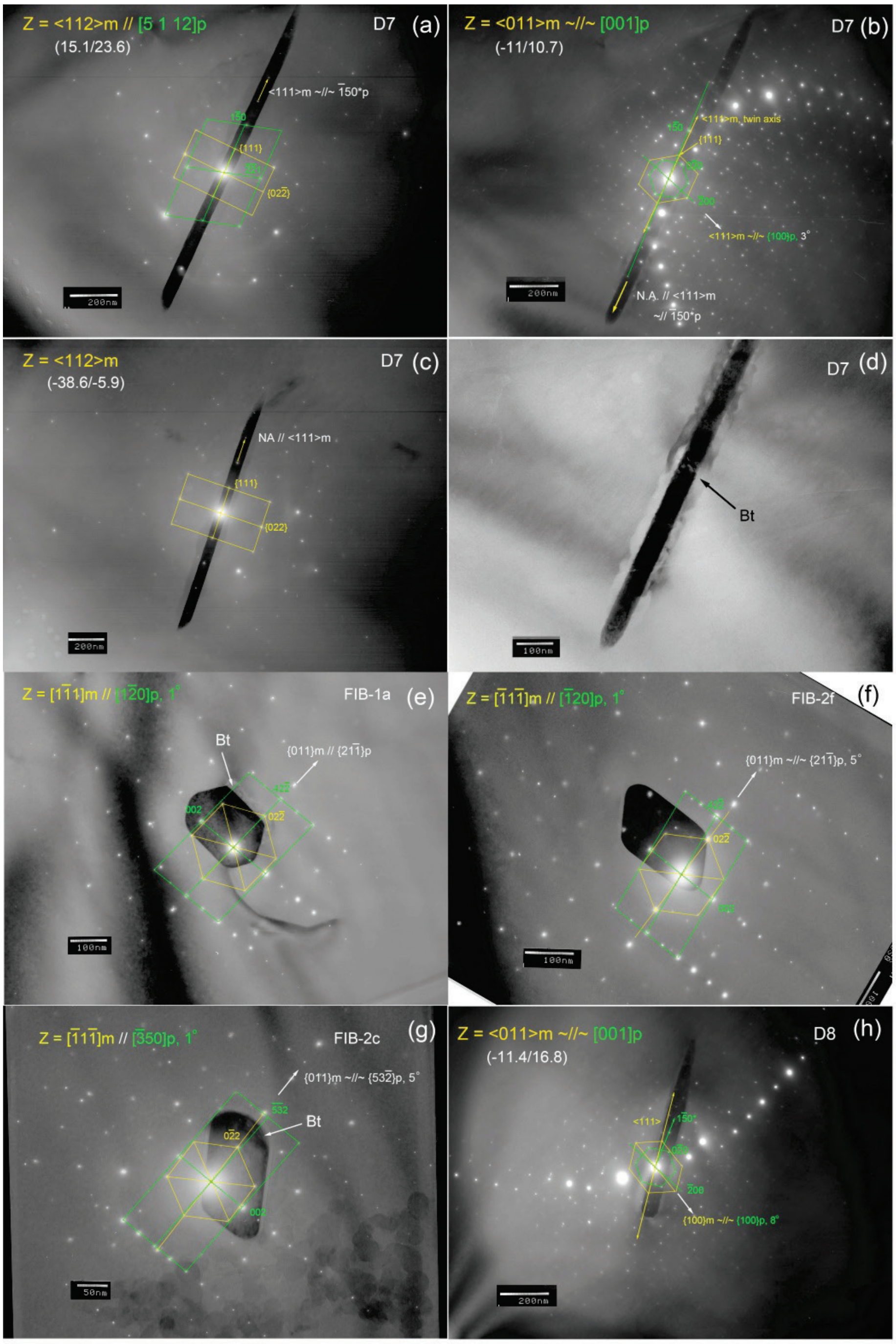

Figure S8

(a,b) TEM BFIs with superimposed SAED patterns of **150***a-needle viewed with needle-axis parallel to image plane showing the exact alignment between needle-axis and <111>$_m$ lattice direction, but~5° off from **150***, (c) BFI+SAED pattern showing the characteristic cross-section of an **150***a-needle bounded by a large set of $\{110\}_m$ facets, (d) BFI and SAED pattern of a **150***b-needle from the same sample domain as the **150***a-needle in (a) showing their spinel-type twin relationship around NA in between, (e) BFI+SAED pattern of **150***b-needle viewed end-on showing the facetted cross-section and the COR: $[11\bar{1}]_m$ // $[352]_p$, $(101)_m$ // $(\bar{1}1\bar{1})_p$, and (f-h) BFI and SAED of **150***r-needles viewed with (f) NA parallel to image plane and (g.h) end-on showing the the resorbed outlines and mica associations.

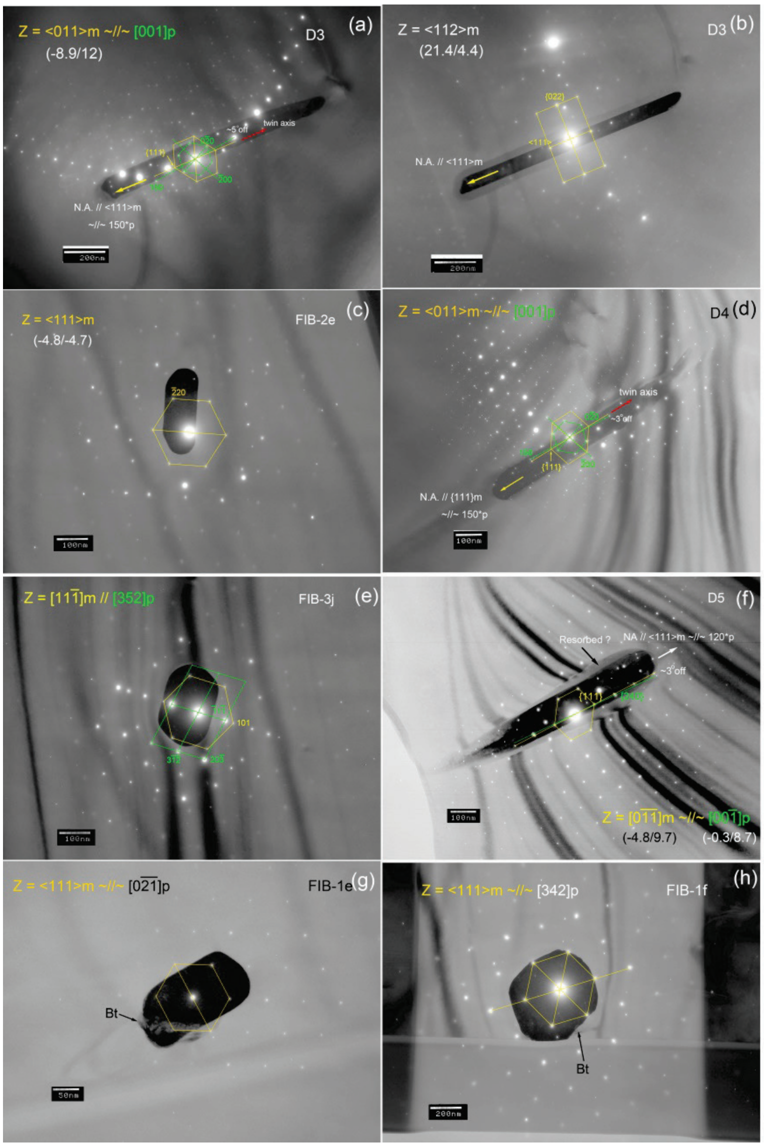

Figure S9

TEM BFI and SAED pattern showing 001 mica plates lying parallel to (a) 112_p, (b) 150p, and (c) 150_p and $\bar{1}50_p$.

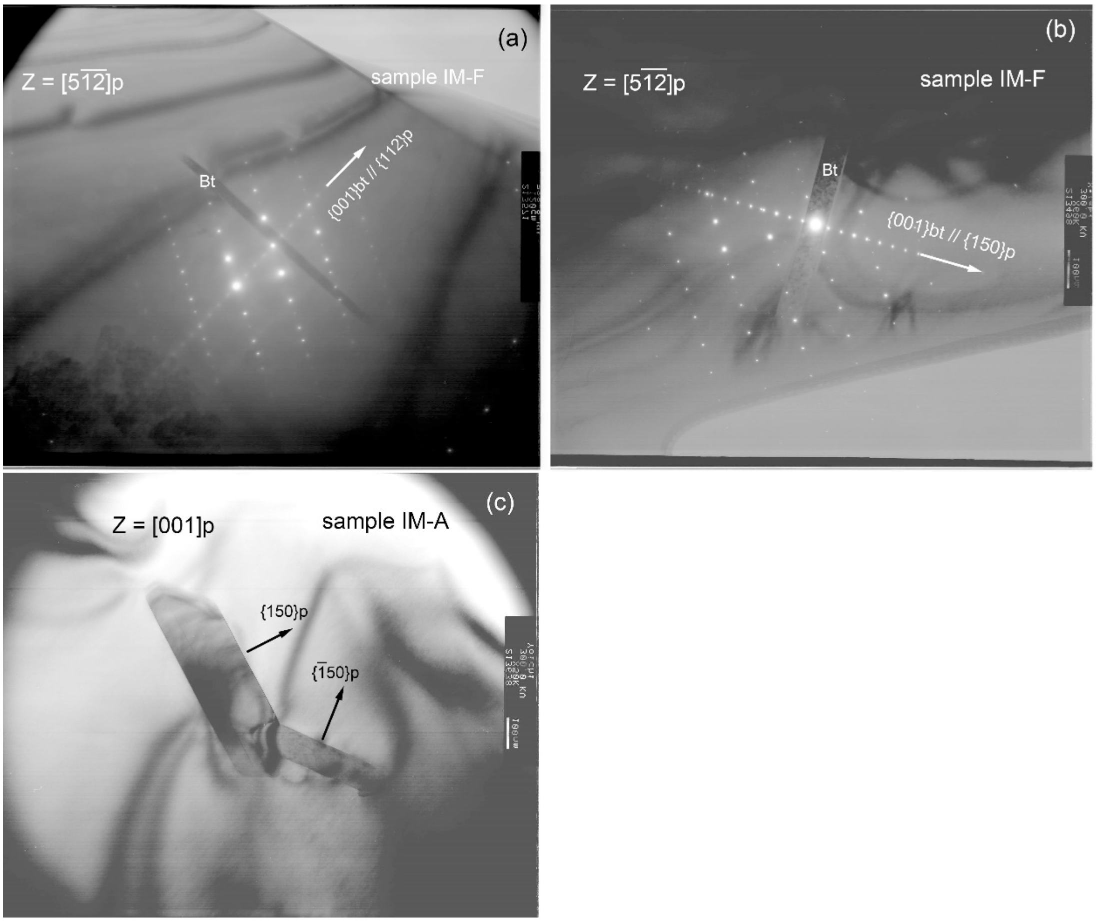

Figure S10

TEM BFIs and corresponding SAED patterns showing quasi-cp $\{150\}_p$ or $\{\bar{1}50\}_p$ oxygen plane of feldspar (f) is aligned with (a,b) quasi-cp $\{100\}_r$ oxygen plane of the $[001]_r$ // $[001]_f$-oriented rod-like rutile (r) inclusion, and (c,d) cp $\{0001\}_i$ oxygen planes of the $[1\bar{1}00]_r$ // $[001]_f$-oriented blade-like ilmenite (i) inclusion in commercial labradorite stones.

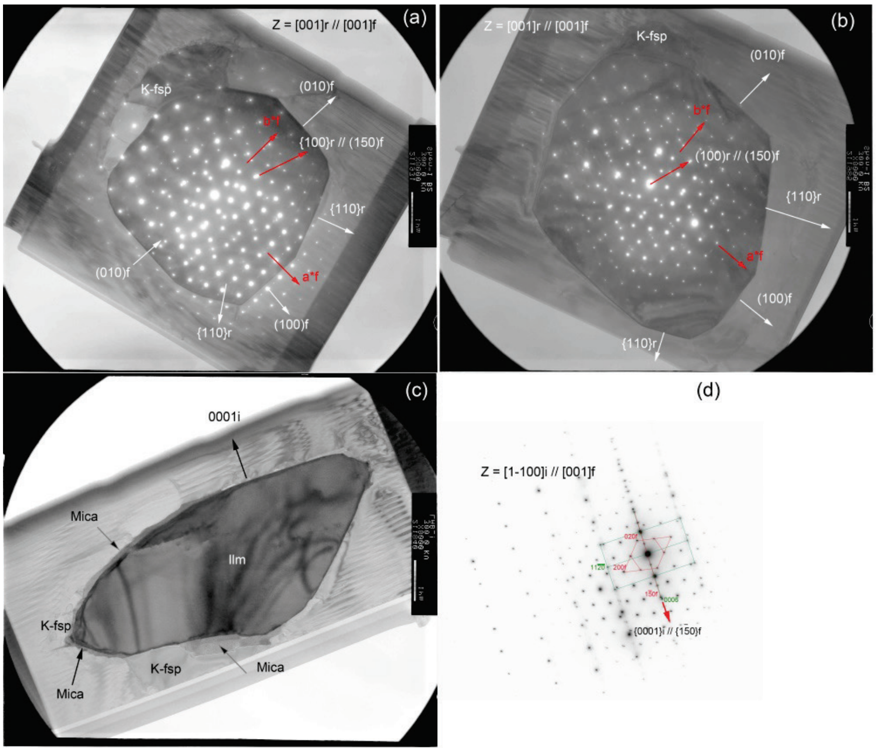

Figure S11

Plagioclase structure projections along (a) $[\bar{5}12]_p$ and (b) $[517]_p$ directions showing TO4 polyhedra bounded by (a) 112_p, 150_p, and $0\bar{4}2_p$ planes, and (b) $\bar{3}12_p$, $\bar{1}50_p$, and $24\bar{2}_p$ plane.

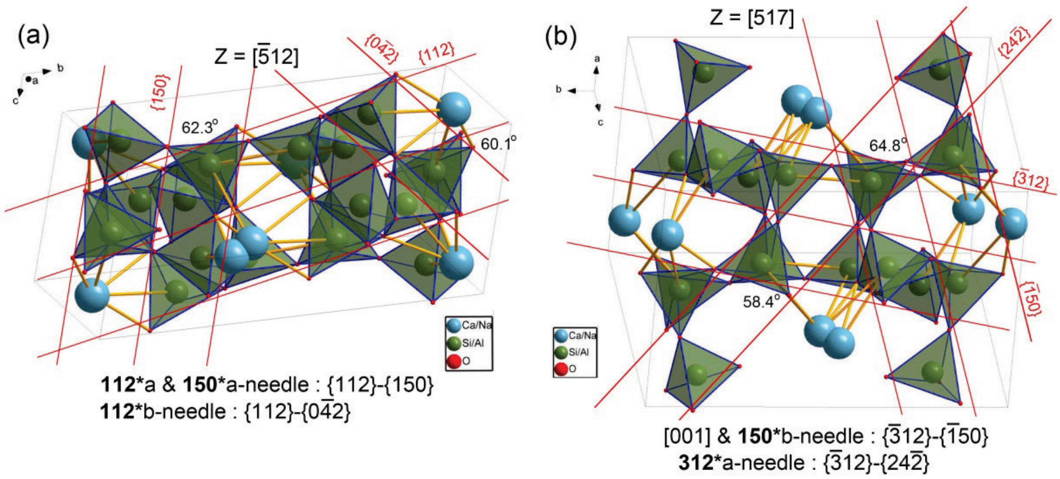

Table S1

The 2D CSL match for the well-defined /aligned lateral facets of magnetite needles in plagioclase

variant	aligned facets aligned directions // NA	$\langle U_1V_1W_1\rangle_p$ / $\langle U_2V_2W_2\rangle_p$: L_{1p} / L_{2p} / ϕ $\langle U_1V_1W_1\rangle_m$ / $\langle U_2V_2W_2\rangle_m$: L_{1m} / L_{2m} / ϕ ε_1* / ε_2 / $\Delta\phi$ $\langle U_1V_1W_1\rangle_m$ / $\langle U_1V_1W_1\rangle_p$: L_1 / L_2 / ε
112*a	$\{011\}_m$ // $\{\bar{1}50\}_p$ NA // $\langle 111\rangle_m$ // $\langle 518\rangle_p$	$\langle 518\rangle_p$ / $\langle \bar{5}\bar{1}8\rangle_p$: 54.13 / 84.68 / 72.21° 4$\langle 111\rangle_m$ / 6$\langle 111\rangle_m$: 58.2 / 87.3 / 70.5° 7.5% / 3.1% / -1.7° 4$\langle 111\rangle_m$ // $\langle 518\rangle_p$: 58.2./ 54.1 / 7.5%
$\bar{3}$12*a	$\{011\}_m$ // $(150)_p$ NA // $\langle 111\rangle_m$ // $\langle \bar{5}12\rangle_p$ NA // $\langle 111\rangle_m$ // $\langle \bar{7}14\rangle_p$	$\langle \bar{5}18\rangle$ / $\langle 5\bar{1}8\rangle$: 83.77 / 55.88 / 72.82° 4$\langle 211\rangle_m$ / 3$\langle 211\rangle_m$: 82.30 / 61.74 / 70.5° -1.8% / 10.5% / 2.32° 7$\langle 111\rangle_m$ // 2$\langle \bar{5}12\rangle_p$: 101.84 / 100.64 / 1.1% 5$\langle 111\rangle_m$ // $\langle \bar{7}14\rangle_p$: 72.7 / 75.08/ -3.2%
[001]	$\{211\}_m$ // $(1\bar{2}0)_p$ (3-4° off) NA // $\langle 011\rangle_m$ // $[001]_p$	3$\langle 001\rangle$ / $\langle \bar{5}\bar{2}8\rangle$: 21.3 / 88.02 / 30° 2$\langle 011\rangle_m$ / 3$\langle 131\rangle_m$: 23.74 / 83.57/ 31.5° 11.5 % / -5.1% / -0.1° 2$\langle 011\rangle_m$ //3$[001]_p$: 23.75 / 21.3 / 11.5%

* $\varepsilon = (L_m - L_p)/L_p$